Investigation of regimes and associated flow structures during impingement of a liquid drop on a liquid pool

Manas Ranjan Behera,[1] Anvith Rao,[1] Anirvan Dasgupta,[2] and Sudipto Chakraborty[1,*]

[1]*Department of Chemical Engineering, Indian Institute of Technology Kharagpur, Kharagpur 721302, India*

[2]*Department of Mechanical Engineering, Indian Institute of Technology Kharagpur, Kharagpur 721302, India*

(Received 6 October 2021; accepted 4 January 2023; published 31 January 2023)

This work describes a numerical investigation of the impact dynamics and outcomes accompanying the impingement of a liquid drop on a liquid pool. A regime map of these outcomes as a function of the governing dimensionless factors is presented. We find that these outcomes are controlled by inertia, surface tension, and viscous forces. Hence, the phenomena are investigated over a wide range of Weber number ($0 \leqslant \mathrm{We} \leqslant 350$) and Ohnesorge number ($0.002 \leqslant \mathrm{Oh} \leqslant 0.020$). Based on the morphologies, these outcomes are distinguished by two regimes, namely coalescence and splashing, which can be further divided into three subregimes, namely partial coalescence, complete coalescence, and regular bubble entrapment. We quantify the phase boundaries between them and illustrate them in We-Oh phase diagrams. Our comprehensive study further reveals that eight salient flow structures are confined in these regions, including four previously reported flow structures: primary ring, secondary ring, jet, blob, and a combination of them. The characteristics of these flow structures along with their genesis are thoroughly examined. The thresholds of these flow structures are also quantified using nondimensional parameters. Subsequently, they are organized in an orderly manner in the phase diagram. This work thus delineates different regimes, subregimes, and their associated flow structures during the impact of a liquid drop on a liquid pool, and it constructs phase boundaries between them.

DOI: 10.1103/PhysRevFluids.8.014002

I. INTRODUCTION

The impact of a liquid drop on a liquid pool has long been of interest due to its fundamental relevance in various natural phenomena [1–6] as well as industrial applications [7]. Depending on the physical properties of fluids and the impact velocity of the drop, two broad regions are identified during the impingement of a liquid drop, namely coalescence and splashing. Generally, the coalescence regime is observed at low impact inertia of the drop. During the coalescence of the liquid drop on a liquid pool, a neck develops at the contact point of the drop and liquid pool. The neck expands fast due to capillary pressure. The expanding neck generates capillary waves that propagate along the drop wall. Simultaneously, the drop liquid drains into the pool due to the excess capillary pressure inside the drop. The draining drop converts to a cylindrical protrusion as the capillary waves converge at the apex of the drop. After reaching a maximum point, the apex height of the cylindrical column retracts vertically, whereas its neck retracts horizontally. Depending on the competition between these horizontal and vertical collapse rates, two major topological changes of the drop are observed above the interface: partial coalescence [8–17], in which the drop coalesces

*Author to whom all correspondence should be addressed: sc@che.iitkgp.ernet.in

 ©2023 American Physical Society

partially with the pool leaving behind secondary droplets, and complete coalescence [18–24], in which the drop merges completely with the pool. Partial coalescence has been studied to gain insight into the pinch-off process and the hydrodynamics of the generated secondary droplets. The boundary between partial coalescence and complete coalescence has been defined in terms of dimensionless parameters, namely, the Reynolds number $\mathrm{Re} = \rho U_d D/\mu$ [16] and the Ohnesorge number $\mathrm{Oh} = \mu/\sqrt{\rho\sigma D}$ [12,13]. Here μ, ρ, and σ denote, respectively, the dynamic viscosity, density, and surface tension of liquid, and U_d and D are the impingement velocity and diameter of the drop. Complete coalescence has always been characterized and studied in terms of the evolution of the vortex ring, which forms below the interface following the coalescence of the drop on a liquid pool [18–28].

With an increase in the impact inertia of the drop, a transition from coalescence to splashing occurs [25,29–37]. When a liquid drop impacts a liquid pool with a very high velocity, a crater with the crown at its periphery is formed, and a central jet arises from the center of the crater during its retraction. The qualitative description of a splash was first elucidated by Worthington [29–32]. It is observed that the speed of the jet is higher than the impact speed of the drop, and it can result in the jet breakup and formation of one or more droplets from its tip. An additional increase of the impact velocity results in the crown fragmenting into smaller droplets. The splashing regime has been studied to define its boundary with the coalescence regime [33,38–40] and to understand the hydrodynamics of the jet and the crown, which has been of considerable interest [37,41].

An important occurrence that is observed in a sharply delimited region of the splashing phenomenon, which has been studied independently in the past, is regular bubble entrapment [33–36,42–46]. Under certain impact conditions, a bubble is entrapped at the bottom of a crater, and as the phenomenon is reproducible, it is termed regular bubble entrapment. It is observed that the entrapment of a bubble is always followed by a thin rapidly rising jet [33]. Pumphrey and Elmore [42] were the first to report the regular bubble entrapment region using the U_d-D map. Oğuz and Prosperetti [43] have replotted the U_d-D map in terms of dimensionless parameters Fr and We, where the lower limit is $\mathrm{We}_l = 41.3\mathrm{Fr}^{0.179}$ and the upper limit is $\mathrm{We}_u = 48.3\mathrm{Fr}^{0.247}$. The Weber number $\mathrm{We} = \rho U_d^2 D/\sigma$ measures the relative importance of inertia force compared to surface tension force. The Froude number is defined as $\mathrm{Fr} = U_d^2/gD$, where g is the acceleration due to gravity. Water has been used as a liquid medium to study regular bubble entrapment. As a result, the viscous damping effect had been neglected until the work of Deng *et al.* [45], who studied the effect of surface tension and viscosity in terms of the Capillary number $\mathrm{Ca} = \mu U_d/\sigma$, and they observed that entrapped bubble size decreases with an increase in Ca. They have determined the threshold of the regular bubble entrapment phenomenon as $\mathrm{Ca} = 0.6$. Chen *et al.* [46] have studied the sole effect of viscosity on the regular bubble entrapment process. They suggested that the viscous damping effect on the propagation of capillary waves increases the lower limit of regular bubble entrapment, whereas the damping effect on the retraction dynamics of the crater raises its upper limit.

There are few reports in the literature describing the conditions under which a transition occurs from coalescence to the splashing regime. Rodriguez and Mesler [25] demarcated the coalescence and splashing regimes using an Fr-Re phase diagram. In the literature [38,39], a critical Weber number $\mathrm{We}_c = 64$ has been defined below which a drop merges with the pool and forms a vortex ring. Above this critical value of We, splashing occurs, a central jet rises from the retracting crater, and the vortex ring vanishes. Rein [33] also postulated that a critical Weber number exists below which coalescence is observed and above which the splashing phenomenon occurs. He also claimed that the generation of a vortex ring and a central jet are, respectively, the criteria of coalescence and splashing. Based on the size of the jet and its tip breakup, as well as the bubble entrapment, Rein [33] ordered the flow structures observed in the splashing regimes. Later, Morton *et al.* [34] and Ray *et al.* [36] showed that a vortex ring and a jet can be observed together in the splashing region. Liow [35] delineated the domain of coalescence, a high-speed jet, and bubble entrapment using a We-Fr phase diagram. Ray *et al.* [36] showed six different types of the phenomenon in the splashing regime using a We-Fr phase diagram.

From this extensive literature on the drop impact on a liquid pool, it can be deduced that there is a wide range of phenomena associated with drop impact dynamics. Nevertheless, the conditions under which a transition occurs from one phenomenon to another continues to be a mystery, and the regime map of these phenomena as a function of the controlling parameters is far from comprehensive. In addition, not all flow structures observed in these regimes have been captured yet as the impact dynamics are studied under limited conditions. The surface tension, inertia, and viscous forces are the key physical forces involved in the drop impact on a liquid pool system. We imply that there have been only a few studies on the influence of viscosity on drop impact dynamics as water has been considered as the drop and pool liquid. As most of the previous works on coalescence, splashing, and bubble entrapment have considered water as the drop and pool liquids, the effect of the variation of the viscosity of liquids on drop impact dynamics has been neglected. Thus, the influence of viscous damping on these regimes has been neglected. The purpose of the present study is to address the aforementioned issues using numerical simulations. An attempt is made here to define each regime and its associated flow structures both qualitatively and quantitatively. For this purpose, a systematic investigation on the drop impact dynamics is carried out with a wide range of We and Oh by varying the physical properties of the liquid and the impingement velocity. Consequently, phase diagrams for regimes and their associated flow structures are plotted in terms of We and Oh. The numerical method, results and discussions, and conclusions are presented in Secs. II–IV.

II. SIMULATION DETAILS

To investigate the impact dynamics during the impingement of a liquid drop on a liquid pool, we carry out numerical simulation using the freely available solver GERRIS [47,48]. This solver has been widely used to study the different phenomena observed during the impingement of a liquid drop on a liquid pool [23,49–53]. It uses the volume-of-fluid (VOF) method to solve the Navier-Stokes equation with dynamic adaptive grid refinement. Here, the algorithm discretizes the two-dimensional domain into $(2^n)^2$ cells, where n corresponds to the level of refinement. The level of refinement states the number and size of the cells in a domain. The dynamic adaptive grid refinement allows us to modify the size of the cell at the desired place, which optimizes the computational time.

A. Computational domain

In the present study, the impingement of a liquid drop on a stationary liquid pool is considered in an axisymmetric computational domain (Fig. 1). Red, light green, and blue markers are used to identify the drop, liquid pool, and air, respectively, in the numerical simulation. The density and viscosity of air were kept fixed at $1.225\,\mathrm{kg/m^3}$ and 0.0181 mPa s, respectively. To study the drop impact dynamics, the impingement velocity of the drop and the properties of the liquid were varied.

B. Governing equations

To ascertain the flow characteristics, GERRIS solves the conservation of mass and momentum equations, which are given by

$$\nabla \cdot u = 0, \tag{1}$$

$$\rho \frac{Du}{Dt} = -\nabla p + \nabla \cdot [\mu(\nabla u + \nabla u^T)] + \sigma\kappa\delta_s\hat{n} + \rho g, \tag{2}$$

where u, t, and p denote the velocity field, time, and pressure, respectively, κ symbolizes the curvature, δ_s represents the Dirac delta function, and $\hat{n}$ is the unit normal at the interface. To track the location of the interface, volume fraction field c is used, which satisfies the following advection equation:

$$\frac{\partial c}{\partial t} + u \cdot \nabla c = 0. \tag{3}$$

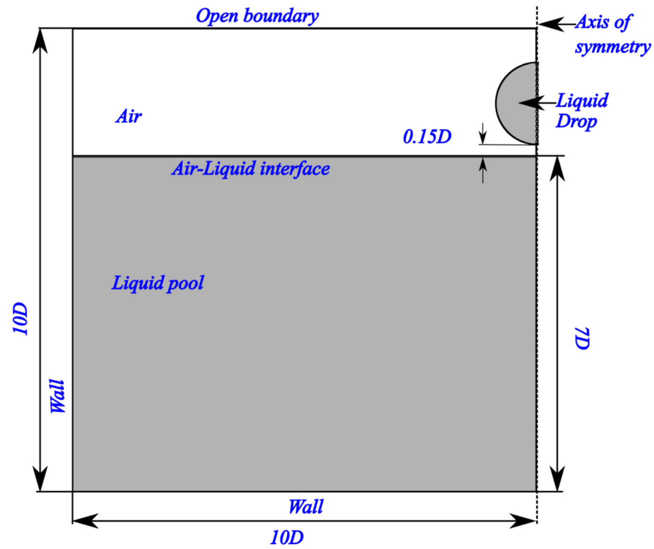

FIG. 1. Schematic diagram of the computational domain representing the impingement of a liquid drop on a stationary liquid pool.

The local density and viscosity are defined as follows:

$$\rho = \rho_1 c + \rho_2(1 - c), \tag{4}$$

$$\mu = \mu_1 c + \mu_2(1-c). \tag{5}$$

Here, indices "1" and "2" indicate liquid and air, respectively. To determine the refinement level of the cell, a grid independence test has been carried out (Appendix A). On the basis of the result, the maximum refinement was taken as 11 (2^{11} cells in each direction) and the minimum refinement was taken as 7 (2^7 cells in each direction). The accuracy of this code was validated in Refs. [23,51]. The validation of the present numerical results is provided in Appendix B.

III. CLASSIFICATION OF REGIMES

Depending upon the choice of impingement conditions and physical properties of the liquid, the impact dynamics and the outcomes can be extremely complex. However, these complex phenomena can be broadly classified into two regimes, namely coalescence and splashing. Based on the topological change above the interface, the coalescence regime is categorized into (i) partial coalescence and (ii) complete coalescence. Similarly, a limited region of the splashing where the regular bubble entrapment is observed is considered as the subregime of splashing. These regimes can be further classified depending on the observation of the different flow structures. Therefore, it is necessary to analyze each regime in the impact process and comprehend the physical aspects behind the observed phenomena. In the present parametric study, we elucidate the subtle interplay of the different forces on the impact outcomes and map out the boundaries between them in the phase diagram.

A. Coalescence regime

During coalescence of a drop, the competition between the vertical and horizontal collapse rate of the cylindrical drop decides whether the drop will pinch off to form a secondary droplet (partial coalescence) or merge completely into the pool (complete coalescence). Pinch-off of a secondary droplet occurs when the inward horizontal movement of the cylindrical drop exceeds its downward vertical movement. The rates of vertical and horizontal collapse are controlled by different forces.

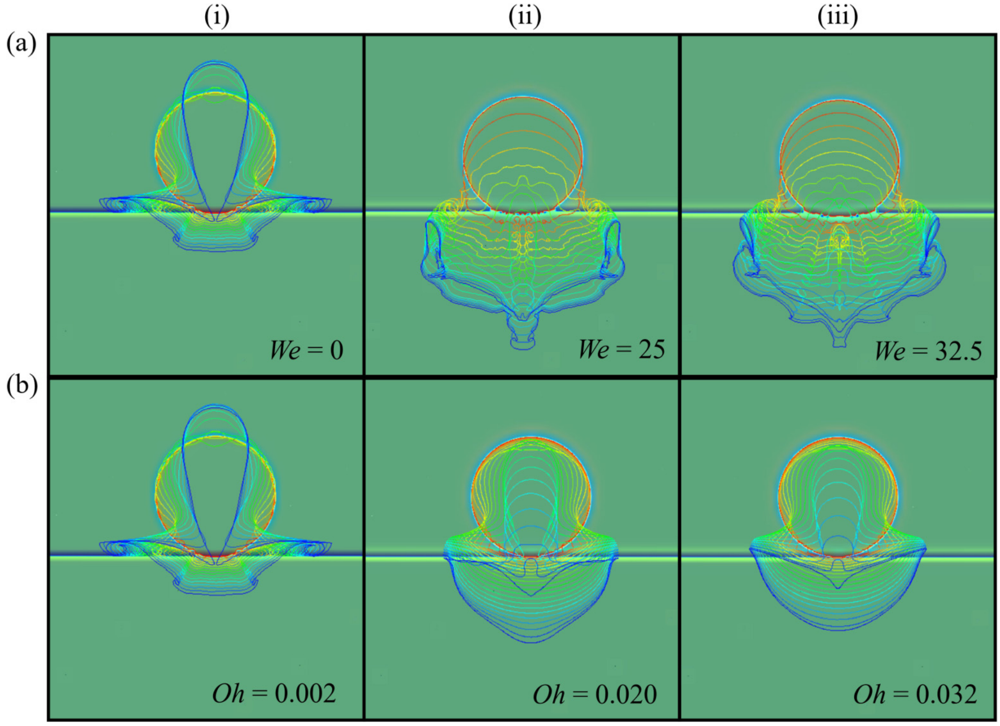

FIG. 2. Effect of (a) We at a constant Oh = 0.002 and (b) Oh at a constant We = 0 on coalescence dynamics during the impingement of a liquid drop on a liquid pool. Here, index (i) represents partial coalescence, whereas indices (ii) and (iii) represent complete coalescence.

Hence, the partial coalescence and complete coalescence regimes have been demarcated using different dimensionless variables in numerous previous studies [8–17]. However, the demarcation as a function of We has not been documented yet. Here, we characterize the partial coalescence and complete coalescence regimes in terms of We and Oh. Before embarking in the multifaceted We-Oh phase diagram at hand, it is useful to study the effect of We and Oh individually. For this purpose, the drop liquid is traced at different time instances for distinct We and Oh, as shown in Fig. 2.

The competitive effect of inertia and surface tension force on the coalescence process is studied in terms of We for a given Oh. Here, the horizontal and vertical collapse rates are controlled by the momentum of the capillary waves and the impact inertia of the drop. As we can see in Fig. 2(a), partial coalescence of the drop is observed at low We compared to complete coalescence of the drop. In the figure, the upward stretching of the liquid column by the capillary waves is evident when We = 0. As a result, the apex height of the drop is greater than its initial diameter. It eventually causes the vertical collapse rate to be slower than the horizontal collapse rate, resulting in the partial coalescence of the drop. The penetration of the drop liquid into the pool increases with the increase in inertia at higher We, which accelerates the downward vertical collapse rate. As it effectively balances out the upward stretching of the liquid column, the increase in We favors the complete coalescence of the drop.

For a specific We, the effect of surface tension and viscous forces are studied in terms of Oh. Here, the degree of the viscous damping effect on the momentum of the capillary waves determines the outcomes of the coalescence process. The capillary wave stretches the liquid column upward as the viscous effect is insignificant at lower Oh [Fig. 2(b)]. Consequently, it causes the vertical collapse rate to be slower than the horizontal collapse rate, and it favors the partial coalescence of the drop. It can be observed from the figure that apex height is always less than the initial diameter of

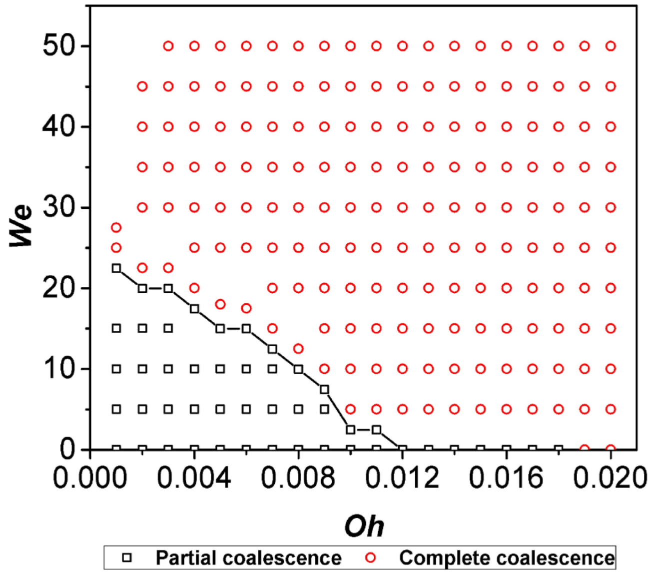

FIG. 3. Oh-We phase diagram identifying the partial coalescence and complete coalescence subregimes.

the drop at higher values of Oh. It signifies that the increase in the viscous damping effect at higher Oh damps the capillary waves responsible for the upward stretching of the liquid column. Thus, the downward vertical collapse starts relatively earlier and prevails over the horizontal collapse. As a result, complete coalescence is observed at higher Oh. Although both We and Oh favor the complete coalescence of a drop, the perturbations are present in higher We while they are absent in larger Oh.

To make such qualitative observations more quantitative, a regime map as a function of We and Oh is generated, as shown in Fig. 3. For a given value of $\mathrm{Oh} < \mathrm{Oh}_{\mathrm{Cpc}}$, the higher values of We favor the complete coalescence of drop. The subscript Cpc describes the critical value of the dimensionless number below which the partial coalescence regime is observed. The penetration of the drop liquid into the pool increases with the increase in the inertia of the drop at higher We. As it effectively balances out the upward stretching of the liquid column, the increase in We thus favors the complete coalescence of the drop. At higher values of Oh for a given $\mathrm{We} < \mathrm{We}_{\mathrm{Cpc}}$, the viscous force damps the momentum of the capillary waves responsible for the upward stretching of the liquid column. Thus, the downward vertical collapse starts relatively earlier and prevails over the horizontal collapse. As a result, complete coalescence is observed at higher Oh. As both We and Oh favor the complete coalescence at their higher values, partial coalescence is very sensitive to We with increasing Oh. The value of $\mathrm{We}_{\mathrm{Cpc}}$ decreases with increasing Oh until a critical value of the Ohnesorge number $\mathrm{Oh}_{\mathrm{Cpc}}$ is reached. When $\mathrm{Oh} \geqslant \mathrm{Oh}_{\mathrm{Cpc}} = 0.019$, only complete coalescence is observed and it is independent of We. The present result is in close agreement with the experimental result ($\mathrm{Oh}_{\mathrm{Cpc}} = 0.018 \pm 0.002$) of Blanchette and Bigioni [13].

1. Flow structures

During the above parametric studies of partial coalescence and complete coalescence, different flow structures below the interface are revealed. Generally, the flow characteristic of the coalescence regime is represented by a single vortex ring [20,33]. Later, Morton *et al.* [34] and Ray *et al.* [36] observed that multiple vortex rings can be formed during the coalescence of a liquid drop. Here, we observe two additional flow structures in the coalescence regime, and we distinguish multiple vortex rings based on their generation mechanism: (F1) blob and secondary ring, (F2) primary ring and secondary ring, (F3) primary ring, and (F4) blob. Furthermore, we find that (F1) blob and

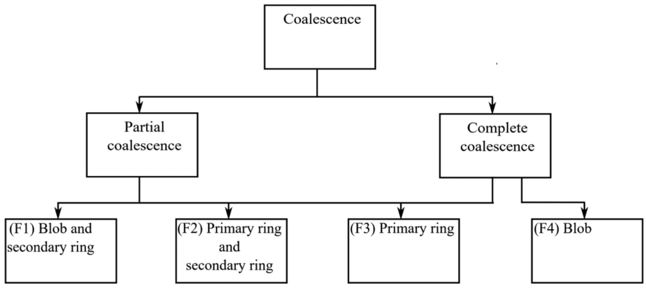

FIG. 4. Block diagram showing the subregimes and associated flow structures of the coalescence regime.

secondary ring, (F2) primary ring and secondary ring, and (F3) primary ring and secondary ring are observed in the partial coalescence subregime, whereas all four flow structures are observed in the complete coalescence subregime, as shown in the block diagram (Fig. 4). By studying the effect of We and Oh, it is found that both of these dimensionless parameters control the genesis of these flow structures. Thus, the thresholds of these flow structures are determined with respect to We and Oh, which aids in organizing these flow structures in the phase diagram (Fig. 5). The time-resolved view of these flow structures with details of their formation are described below.

At a negligible impact velocity of the drop (We $\leqslant 10$) and Oh $<$ $\mathrm{Oh}_{\mathrm{Csr}}$, the flow structure (F1) blob and secondary ring is found. Here, the subscript Csr depicts the critical value of the dimensionless number below which the secondary ring is observed. This flow structure is observed in both the complete coalescence (Fig. 6) and the partial coalescence subregimes (see Fig. S1 in the Supplemental Material [54]). When a drop coalesces with the pool at a very low impact velocity, the

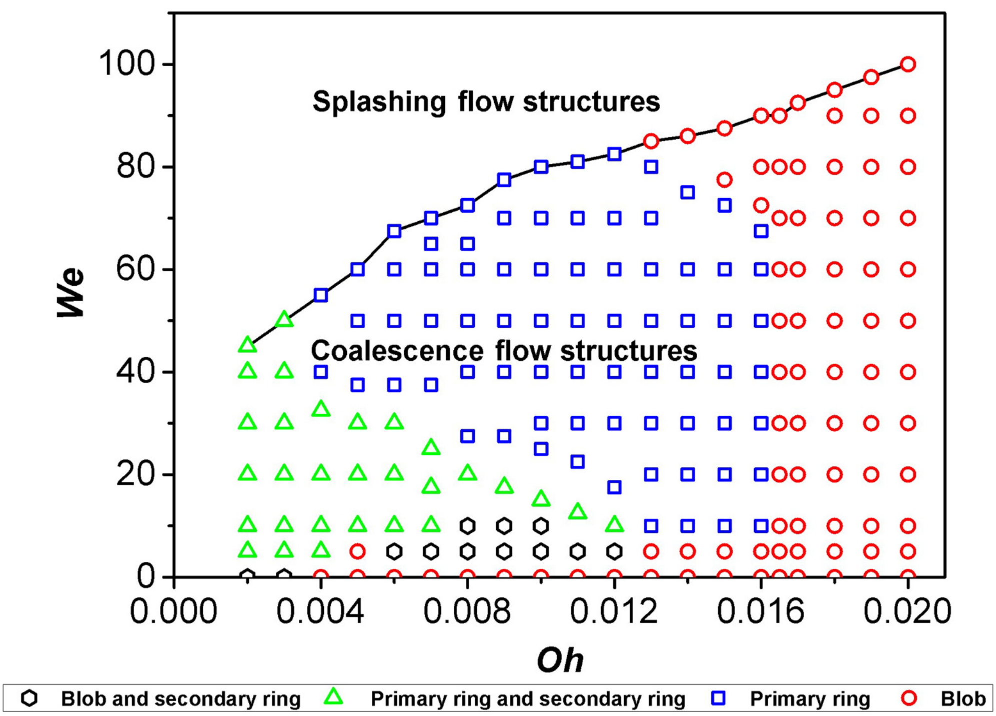

FIG. 5. We-Oh phase diagram of flow structures observes in the partial coalescence and complete coalescence subregimes.

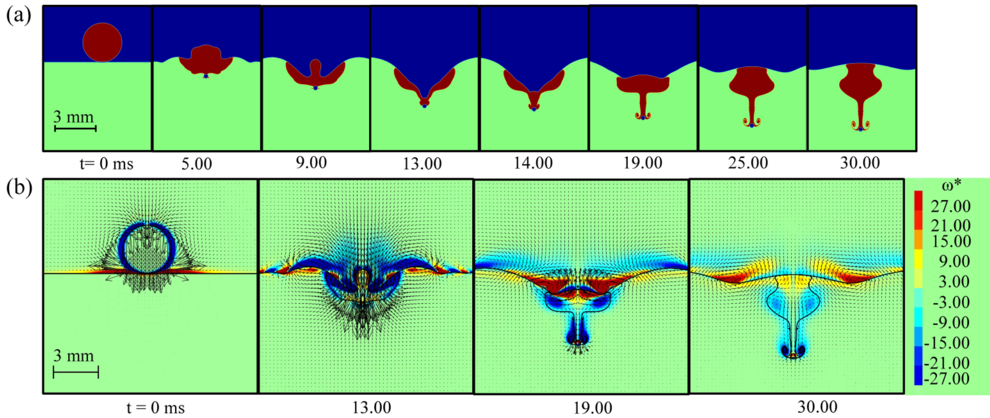

FIG. 6. (a) Flow structure characterized by the formation of a blob and a secondary ring, with (b) the corresponding vorticity contour and velocity vector plot (Oh = 0.0080, We = 10). The parameter $\omega* = \frac{\omega}{U_d/L}$ is the dimensionless vorticity, ω is the vorticity at any time t, and L is the length of the computational domain.

penetrated liquid distributes along the wall of the crater and forms a blob. The remaining portion of the drop liquid in the form of a liquid column penetrates deeper into the pool through the vertex of the crater, and a secondary vortex ring forms out of it due to the shear instability between the pool liquid and the drop liquid.

With the increase in the impingement velocity of the drop for Oh $<$ $\mathrm{Oh_{Csr}}$, the flow structure (F2) primary ring and secondary ring is observed (Fig. 7). This flow structure is witnessed in both the complete coalescence (Fig. 7) and partial coalescence (see Fig. S2 in the Supplemental Material [54]) subregimes. Generally, when the liquid drop impinges on a liquid pool, the impact causes the pool liquid to climb up the drop wall and the drop liquid to penetrate the pool. Thus, a velocity gradient forms at the curved surface of the drop, which causes the favorable condition for the generation of the vortex [23]. This is the origin of the primary vortex ring. The generated primary vortex, along with the drop liquid, penetrates the pool. The primary vortex carries the drop liquid distributed along the wall of the crater and rapidly organizes into a primary vortex ring during the retraction of the crater. As discussed earlier, the liquid column penetrates the pool through the vertex of the crater and forms a secondary ring.

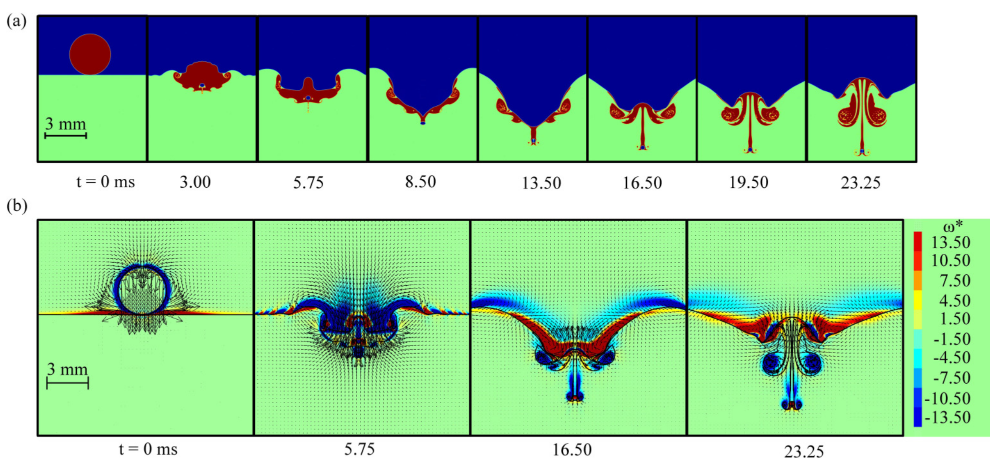

FIG. 7. (a) Flow structure characterized by the formation of a primary ring and a secondary ring, with (b) the corresponding vorticity contour and velocity vector plot (Oh = 0.002, We = 32.5).

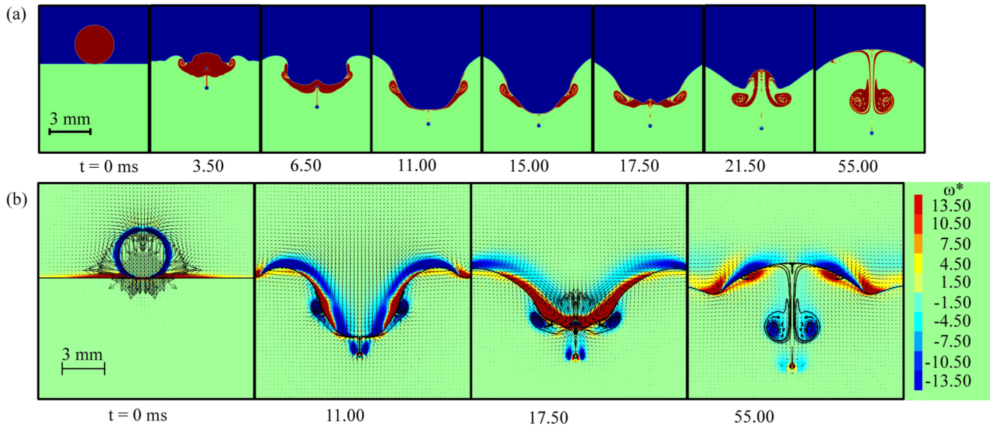

FIG. 8. (a) Flow structure characterized by the formation of a primary ring, with (b) the corresponding vorticity contour and the velocity vector plot (Oh = 0.0043, We = 45).

Either with the increase in We ($\geqslant We_{Csr}$) or Oh ($\geqslant Oh_{Csr}$), the transition occurs from the flow structure (F2) primary ring and secondary ring to the (F3) primary ring (Fig. 5). This flow structure is found only in the complete coalescence subregime, as elucidated in Fig. 8. The increase in inertia at higher We accelerates the drainage rate of the drop liquid into the pool, and consequently the apex height of the liquid column decreases. Thus, the portion of drop liquid that forms a secondary ring decreases at the vertex of the crater. When We increases to a critical value We_{Csr}, the drop liquid is barely present at the vertex of the crater to form the secondary ring. Hence, only the primary vortex ring is observed. Similarly, an increase in Oh for a specific We ($< We_{Csr}$) reduces the apex height of the column since the viscous dissipation damps the momentum of the capillary waves responsible for the upward stretching of the liquid column. It also retards the relative tangential velocity between the liquids of the drop and the pool. As large We and Oh hinder the formation of the secondary ring, We_{Csr} decreases with increasing Oh. When $Oh \geqslant Oh_{Csr} = 0.013$, the strong viscous dissipation impedes the formation of the secondary ring. Hence, only the primary ring is observed irrespective of the value of We, as shown in the phase diagram.

The formation of the primary vortex ring and its hydrodynamics are always a point of discussion in the literature, but an important question remains unanswered: what if both the primary ring and the secondary ring do not form in the coalescence regime? From the phase diagram, it is clear that neither the primary ring nor the secondary ring is observed at specific combinations of We and Oh, and the penetrated drop liquid forms only the (F4) blob flow structure inside the pool. This flow structure is found in both the partial coalescence (see Fig. S3 of the Supplemental Material [54]) and complete coalescence subregimes (Fig. 9). It is prominently observed when $Oh \geqslant Oh_{Cpr} = 0.0165$ as the viscous dissipation strongly damps the momentum of the pool liquid, and it cannot penetrate the drop effectively for the vortical entrapment of the pool liquid with the drop liquid. Thus, the generation of the primary vortex and the formation of the primary vortex ring are inhibited. Although only the blob structure is observed in this range of Oh, it is sensitive to We as a jet appears at very high We. The criteria of jet formation and its associated flow structures are discussed in the next section.

B. Splashing regime

As the impact inertia of the drop increases, the transition occurs from partial coalescence, through a complete coalescence subregime, and finally to a splashing regime. As the drop impacts the pool with high inertia, a deep crater forms, followed by a central jet known as a Worthington jet. Hitherto, the phase boundary between the coalescence and splashing regimes has been characterized in terms

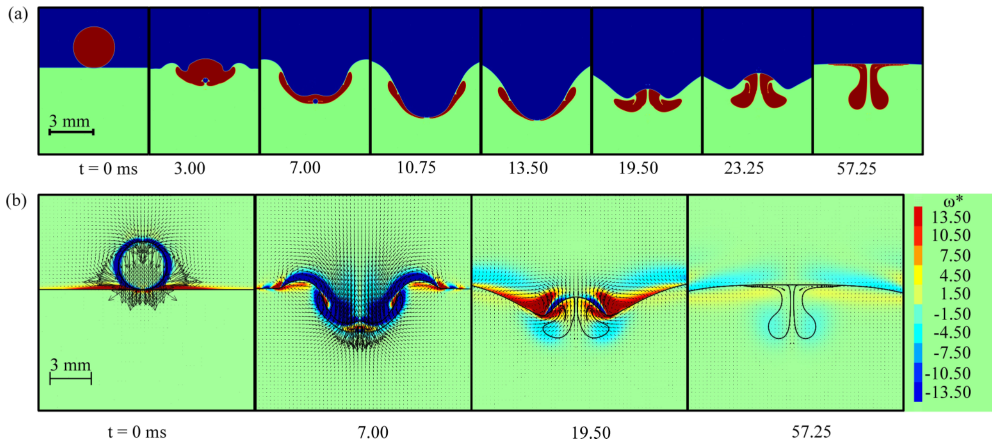

FIG. 9. (a) Flow structure characterized by the formation of a blob, with (b) the corresponding vorticity contour and the velocity vector plot (Oh = 0.0165, We = 43).

of a critical Weber number $\mathrm{We}_{\mathrm{Cco}} = 64$ [38,39]. It has been claimed that below this $\mathrm{We}_{\mathrm{Cco}}$, the drop coalesces into the pool liquid and a vortex ring is formed, and above this $\mathrm{We}_{\mathrm{Cco}}$, the vortex ring vanishes and a jet is observed [38,39]. As shown in Fig. 10, there is indeed a $\mathrm{We}_{\mathrm{Cco}}$ that characterizes the phase boundary between complete coalescence and splashing, but it varies with the Ohnesorge number, as revealed in the present study: $\mathrm{We}_{\mathrm{Cco}} = 363.5\mathrm{Oh}^{0.321}$ for $0.002 \leqslant \mathrm{Oh} \leqslant 0.020$. Below $\mathrm{We}_{\mathrm{Cco}}$, the coalescence regime exists. However, this limit does not demarcate the boundary between the observation of a vortex ring and a jet, which is elucidated in detail in the next section.

1. Flow structures

In the literature, the flow structures of the splashing regimes have been characterized in terms of the thickness of the jet and the breakup of the jet tip into droplets [33,35,36]. They have been presented in the We-Fr regime map. Using numerical simulation, Morton *et al.* [34] have observed

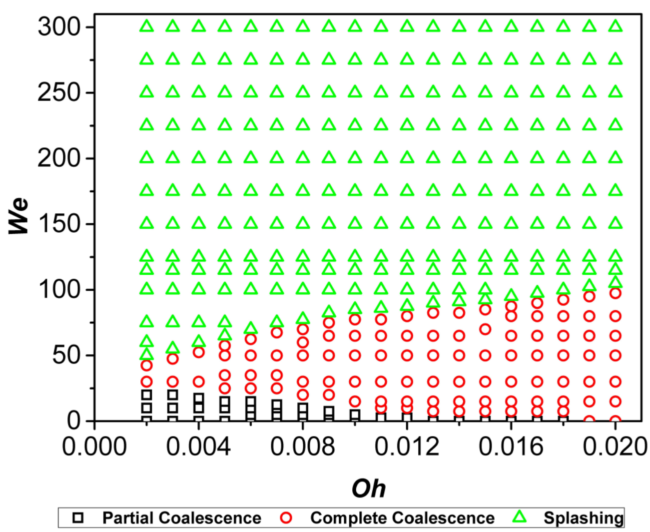

FIG. 10. Phase diagram showing the splashing regime along with subregimes of the coalescence regime in We-Oh parameter space.

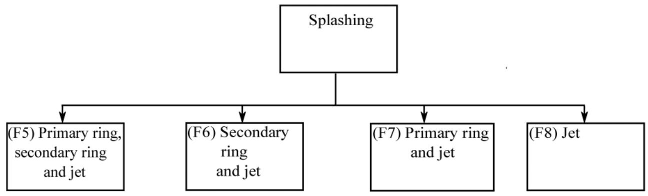

FIG. 11. Block diagram showing flow structures of the splashing regime.

the jet with a small vortex ring (which is described as a secondary ring here) in the splashing regime. As shown in the block diagram (Fig. 11), along with previously reported flow structures, namely the (F8) jet and the (F6) secondary ring and jet, we observed two additional flow structures during our extensive investigation of the splashing regime: the (F5) primary ring, secondary ring, and jet, and the (F7) primary ring and jet. It is observed that the dynamics of the retracting crater plays a key role in the formation as well as the inhibition of these flow structures. As the jet is a common feature observed in all flow structures of the splashing regime, the formation of the jet can be considered as the only criterion of the splashing regime that can distinguish the boundary between coalescence and splashing. To show the phase diagram of these flow structures as a function of We and Oh, and to comprehend the transition of flow structures present in the coalescence regime to that observed in the splashing regime, the complete spectrum of the flow structures obtained in both the coalescence and splashing regimes is presented in the We-Oh plane, as shown in Fig. 12.

For $\mathrm{We} \geqslant \mathrm{We}_{\mathrm{Cco}}$ and $0.002 \leqslant \mathrm{Oh} \leqslant 0.008$, the flow structure (F5) primary ring, secondary ring, and jet is observed in the splashing regime as shown in the phase diagram (Fig. 12). If we look into the transition from the coalescence to the splashing regime, a shift occurs from the (F2) primary ring and secondary ring in the coalescence regime to the (F5) primary ring, secondary ring, and jet in the splashing regime (Fig. 12). Although it is observed at low We in the splashing regime, the impact

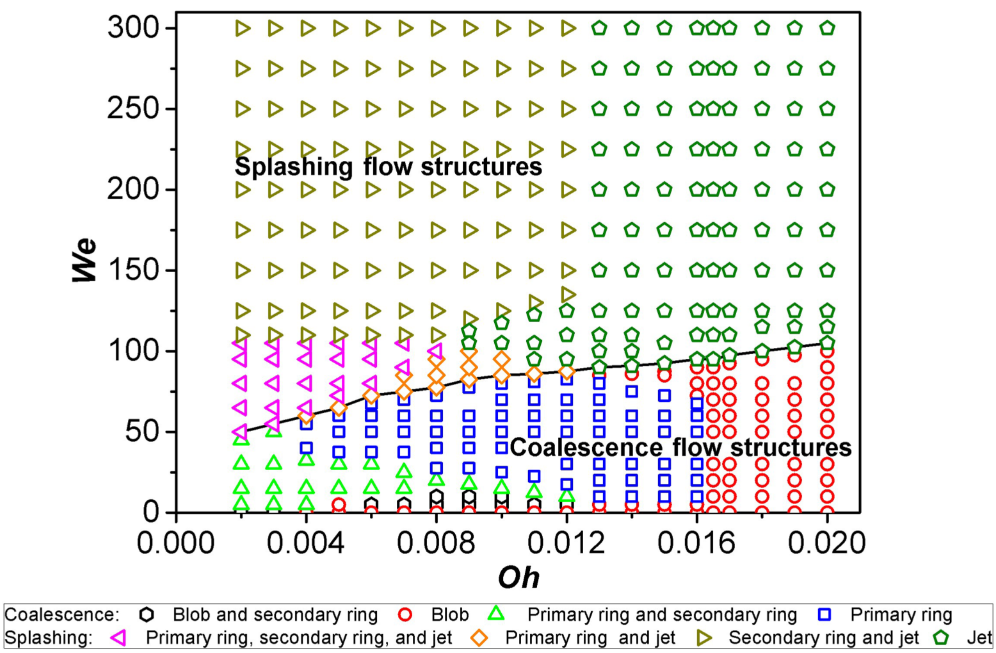

FIG. 12. We-Oh phase diagram showing the different flow structures of the coalescence and splashing regimes.

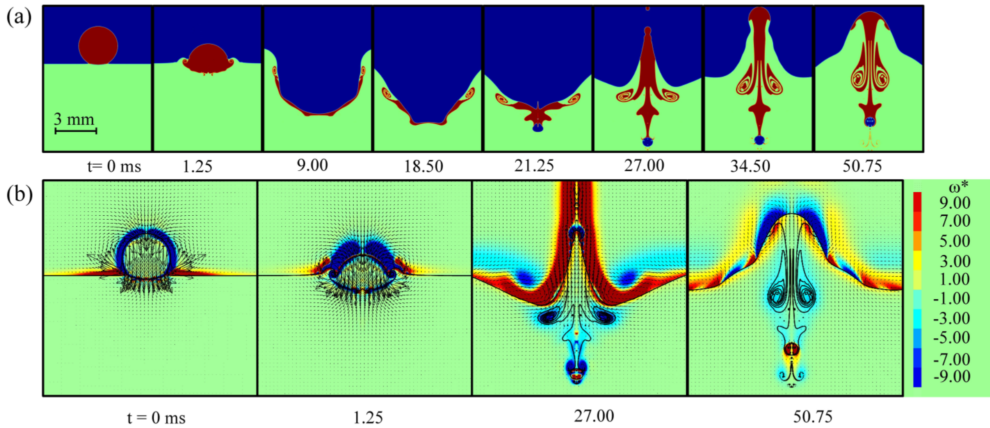

FIG. 13. (a) Flow structure characterized by the formation of a jet, a primary ring, and a secondary ring, with (b) the corresponding vorticity contour and the velocity vector plot (Oh = 0.0043, We = 98).

inertia is enough to produce a central jet from the retracting crater, as shown in Fig. 13. It can be observed from the figure that a small ring also appears deeper in the pool, whose genesis can also be found to be associated with the retracting crater. A curved surface is formed at the bottom of the retracting crater. The relative motion of the drop and pool liquids creates a relative tangential flow near the curved surface. This results in the generation of the second vortex, which moves downward into the pool as a second vortex ring, referred to as the secondary ring.

Upon further increasing We, the flow structure shifts from the (F5) primary ring, secondary ring, and jet to the (F6) secondary ring and jet (Fig. 14). Due to the increase in inertia, the retracting crater not only forms a jet but also engulfs the entire vortex ring. On the other hand, it favors the formation of the secondary ring as the shear instability around the crater base increases.

For $0.004 \leqslant \mathrm{Oh} \leqslant 0.012$, the splashing regime starts with the (F7) primary ring and jet instead of the (F5) primary ring, secondary ring, and jet flow structure (Fig. 15). High viscous dissipation suppresses the relative tangential flow responsible for the generation of the secondary ring. In this range of Oh, the shift occurs from the flow structure (F3) primary ring in the coalescence regime to the (F7) primary ring and jet in the splashing regime (Fig. 12).

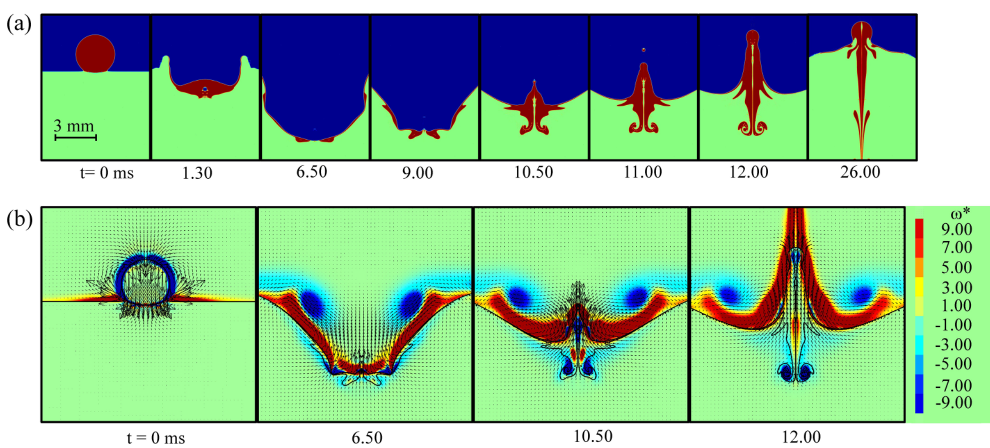

FIG. 14. (a) Flow structure characterized by the formation of a jet and a secondary ring, with (b) the corresponding vorticity contour and the velocity vector plot (Oh = 0.0043, We = 150).

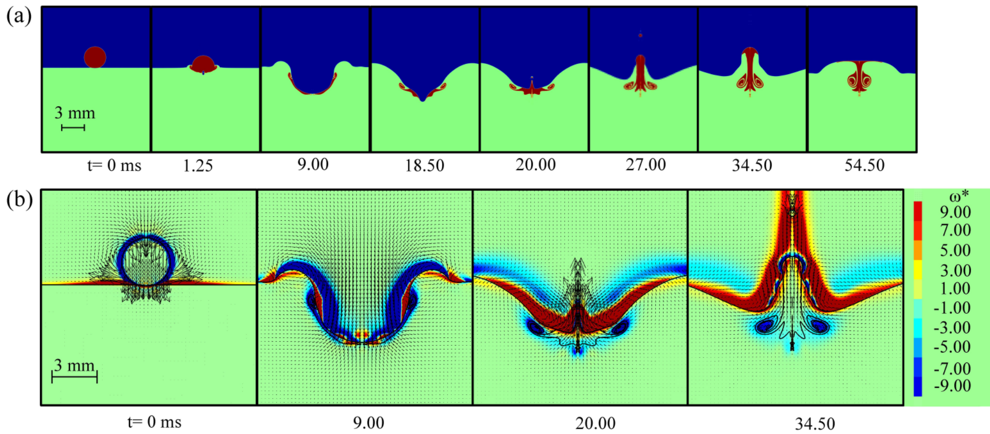

FIG. 15. (a) Flow structure characterized by the formation of a jet and a primary ring, with (b) the corresponding vorticity contour and the velocity vector plot (Oh = 0.0063, We = 75).

With the increase in We at Oh $\geqslant 0.009$, the flow structure transitions from the (F7) primary ring and jet to the (F8) jet (Fig. 12). The retracting crater swallows the vortex ring at the higher impact inertia of the drop, and hence only a jet is witnessed. Further increase in the impact inertia of the drop causes the emergence of the flow structure (F6) secondary ring and jet in the range $0.009 \leqslant$ Oh < 0.013. When Oh $\geqslant 0.013$, the strong viscous dissipation inhibits the formation of the secondary ring, and hence only the (F8) jet flow structure is observed in the splashing regime irrespective of the value of We (Fig. 16).

C. Regular bubble entrapment phenomenon

The regular bubble entrapment is a unique phenomenon that only occurs in a limited domain of the splashing phenomenon but has been studied independently [1,6,36,42,43,45,46]. The crater dynamics plays a key role in the occurrence of the bubble entrapment process. The crater that develops during the impact of a liquid drop on the liquid pool retracts after reaching a maximum crater width, followed by a maximum crater depth. When the crater reaches its maximum width,

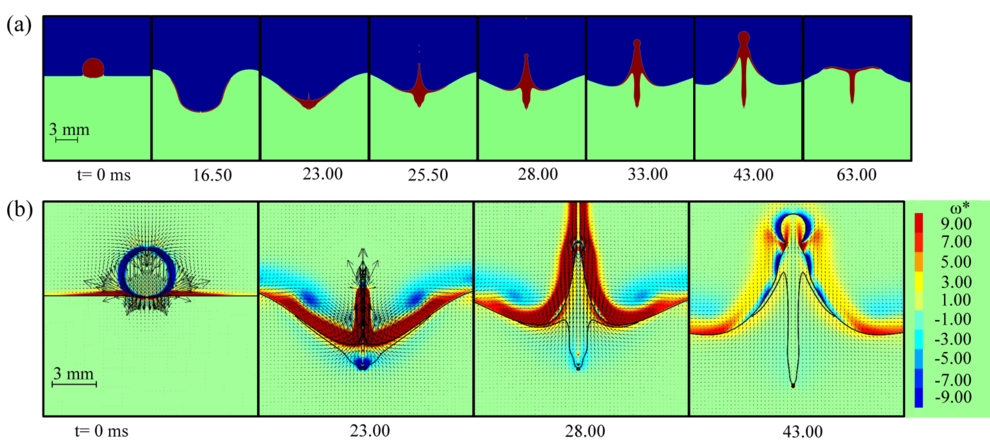

FIG. 16. Flow structure characterized by the formation of jet, with (b) the corresponding vorticity contour and the velocity vector plot (Oh = 0.0165, We = 136).

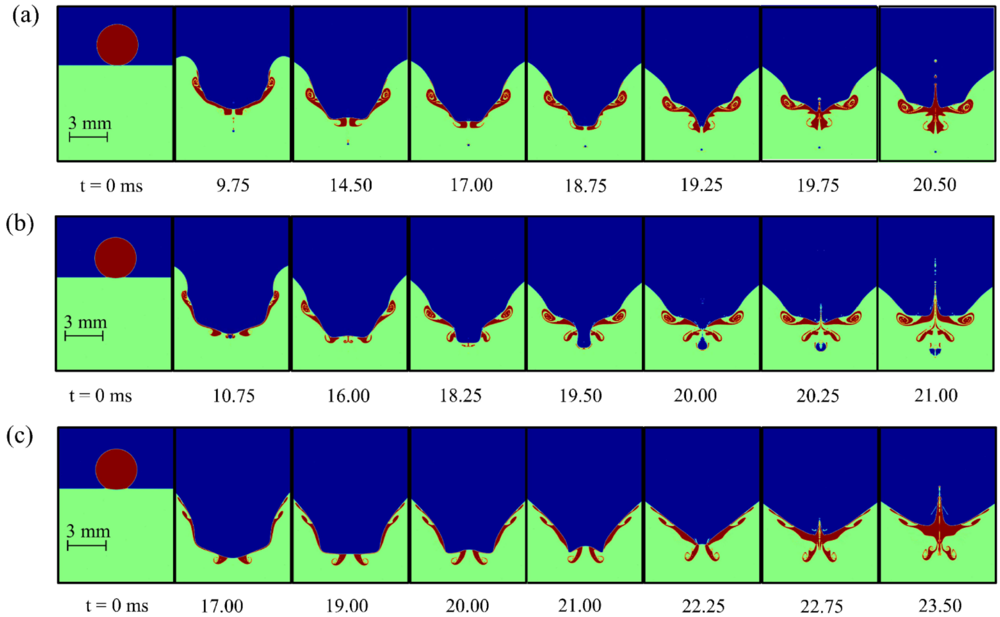

FIG. 17. Flow characteristics (a) below (Oh = 0.002, We = 50), (b) within (Oh = 0.002, We = 80), and (c) above (Oh = 0.002, We = 110) the regular bubble entrapment region.

the sidewalls retract towards the symmetry axis. During the retraction of the sidewalls, the crater reaches a maximum depth, followed by an upward retraction of the crater base. From the present study, we find that the occurrence of regular bubble entrapment is governed by the competition between the rate of upward and horizontal retraction of the crater. When the horizontal retraction rate dominates over the upward retraction rate, the sidewalls merge at the symmetry axis and an air bubble is entrapped, followed by its pinch-off [Fig. 17(b)].

Before studying the different impact conditions on the regular bubble entrapment region, it is necessary to elucidate the difference between the flow structures inside and outside the region of regular bubble entrapment. For that purpose, the impact conditions below (Oh = 0.0022, We = 50), within (Oh = 0.0022, We = 80), and above (Oh = 0.0022, We = 110) the regular bubble entrapment region are illustrated in Fig. 17. Below the regular bubble entrapment region [Fig. 17(a)], a V shape forms near the crater base (t = 19.25 ms) as the sidewall of the crater moves inwards due to the capillary waves. However, the regular entrapment of the bubble is not observed as the sidewalls do not have enough momentum to retract farther towards the symmetry axis and merge. Subsequently, the crater base retracts and forms a jet (t = 19.75 ms). In the bubble entrapment region [Fig. 17(b)], a U-shaped bulge forms as the rate of retraction of the sidewall is quite high. Consequently, the bulge detaches from the crater in the form of an entrapped bubble as the sidewalls intersect at the symmetry axis (t = 19.25 ms) before the start of the retraction of the crater base. For the impact condition (Oh = 0.0022, We = 110), which is above the regular bubble entrapment region [Fig. 17(c)], the retraction of the crater base starts before the formation of the bulge (t = 20.00 ms). Here, the retraction rate of the crater base is quite high as compared to its sidewalls. Thus, the bubble cannot be entrapped as the sidewalls converge at the crater base instead of above the crater base (t = 22.25 ms). As shown in the figure, the jet that forms within the regular bubble entrapment region is thinner than that below and above the regular bubble entrapment regions.

According to conventional considerations, two parameters govern the regular bubble entrapment, namely drop diameter and impact velocity [42,43]. In Fig. 18, the shaded region represents the regular bubble entrapment region reported by Oğuz and Prosperetti [43] using pure water as the

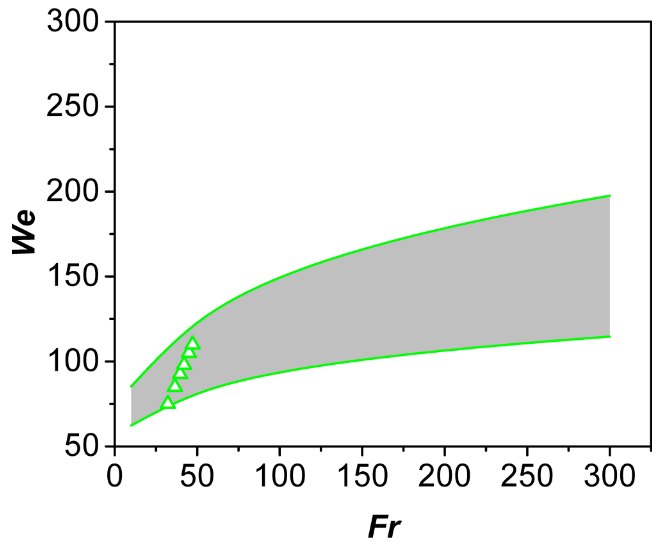

FIG. 18. Shaded area in the We-Fr phase diagram represents the regular entrapment region defined by Oğuz and Prosperetti [43].

liquid medium, where the lower limit is $\mathrm{We}_l = 41.3\mathrm{Fr}^{0.179}$ and the upper limit is $\mathrm{We}_u = 48.3\mathrm{Fr}^{0.247}$. To corroborate with the results of Oğuz and Prosperetti [43], we determine the data points that lie in the proposed regular bubble entrapment region using the properties of water. The data points were obtained by varying the impact velocity of the drop and keeping the diameter of the drop constant. As we can see in Fig. 18, our lower limit is well in line with the lower limit reported by Oğuz and Prosperetti [43]. However, our upper limit differs slightly from the reported upper limit.

Although the mechanism of regular bubble entrapment has been a subject of research for the past two decades, only a few studies [45,46] describe the effect of viscous damping on the regular bubble entrapment phenomenon. From our analysis on the occurrence of the regular bubble entrapment phenomenon, we find that the interplay of viscosity, surface tension, and inertia plays a crucial role in the dynamics of the entrapment process. By varying the inertia, surface tension, and viscosity of the drop liquid over a broad range, novel threshold criteria of the regular bubble entrapment regime are obtained as shown in the cross-hatched region of the We-Oh phase diagram of Fig. 19. The lower and upper limits are, respectively, determined as $\mathrm{We}_l = 516.6\mathrm{Oh}^{0.273}$ and $\mathrm{We}_u = 694.1\mathrm{Oh}^{0.391}$ for $0.002 \leqslant \mathrm{Oh} \leqslant 0.020$. As we can see in the figure, the regular bubble entrapment region is observed near the lower limit of splashing, and both the lower and upper limits of the regular bubble entrapment region increase with the increase in Oh.

To understand the function of each criterion, a systematic investigation has been performed. The effect of Oh on the regular bubble entrapment dynamics is investigated by examining the temporal evolution of the crater shape for a given We = 110. As shown in Fig. 20, regular bubble entrapment is observed in Oh = 0.0043 and 0.0083, whereas it is not evident in Oh = 0.002 and 0.0165. At low Oh (=0.002), which is above the bubble entrapment regime, the effect of viscous damping is negligible. As we can see in Fig. 20(a), the shape of the crater base changes from concave upward to downward, and then it retracts in the upward direction. The retraction of the crater base is higher compared to the cases with higher Oh. As the rate of retraction of the crater base is quite high compared to the rate of retraction of the sidewalls, the bubble cannot be captured. The sidewalls converge at the crater base and form a thick jet at the symmetry axis. When Oh increases to 0.0043 [Fig. 20(b)], the crater shape does not change from concave upward nor does it retract upward. In addition, the retracting sidewalls push the crater base downward. As there is no retraction of the crater base upward, the convergence point of the sidewalls is above the crater base and it leads to

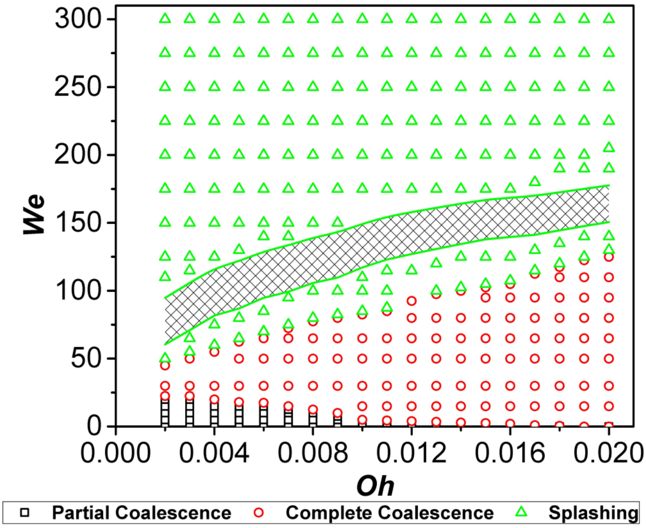

FIG. 19. The We-Oh plot showing the different subregimes of the coalescence and splashing regimes.

entrapment of the bubble. When Oh increases further to 0.0083 [Fig. 20(c)], the crater base remains nearly motionless until the convergence of the sidewalls and the entrapment of the bubble occurs. At very high Oh ($=0.0165$), the higher viscosity damps the retraction of the sidewalls towards the symmetry axis as well as the retraction of the crater base [Fig. 20(d)]. Consequently, the sidewalls

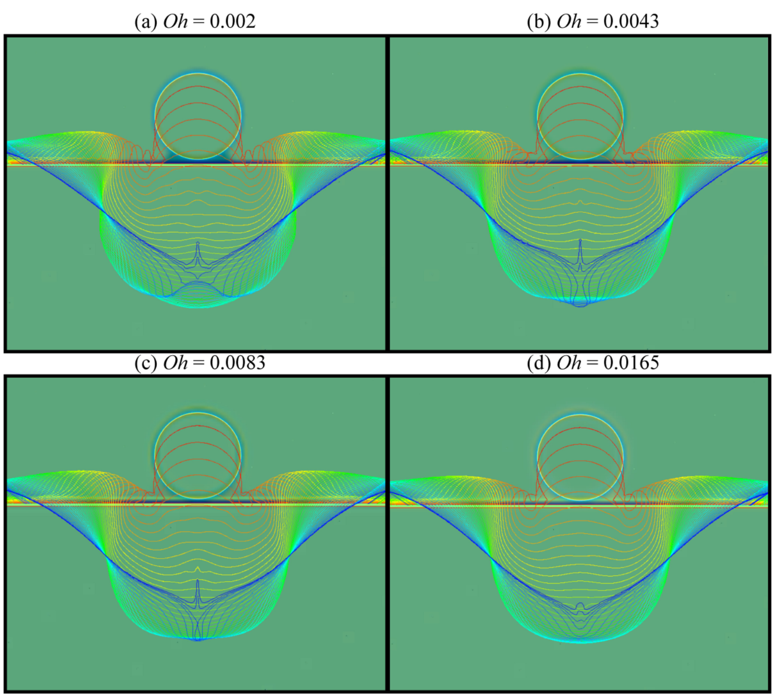

FIG. 20. Temporal evolution of a crater for a given We $=$ 110: (a) Oh $=$ 0.002, (b) Oh $=$ 0.0043, (c) Oh $=$ 0.0083, and (d) Oh $=$ 0.0165.

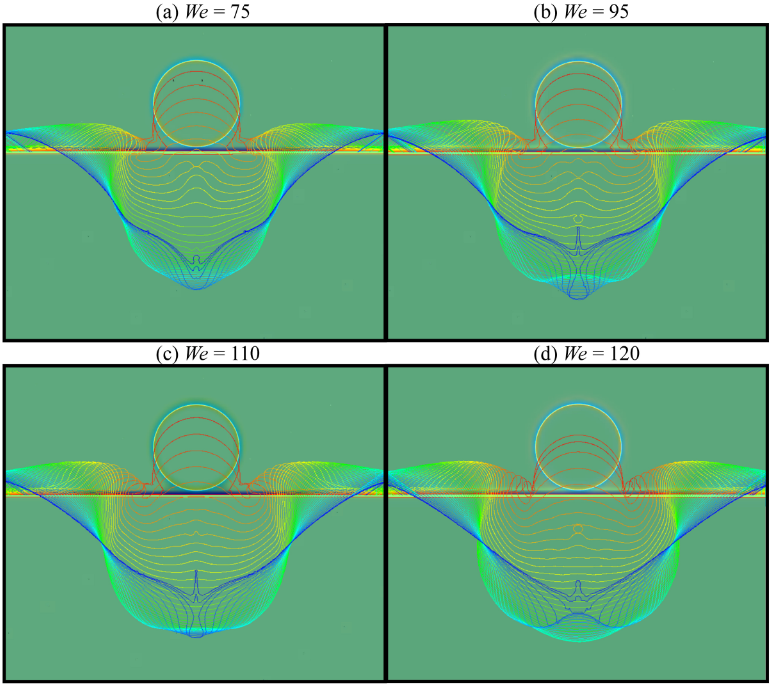

FIG. 21. Temporal evolution of a crater for a given Oh = 0.0043: (a) We = 75, (b) We = 95, (c) We = 110, and (d) We = 120.

cannot form the bulge, and the crater retracts upward uniformly due to the gravitational potential energy.

To explore the influence of We on the regular bubble entrapment dynamics, the temporal evolution of the crater shape for different We at a given Oh = 0.002 is analyzed (Fig. 21). Due to the low inertia of the impact drop at We = 75, the crater base does not retract with a concave down shape, nor do the sidewalls retract sufficiently to merge at the symmetry axis. Consequently, the crater retracts uniformly without a bubble entrapment and forms a thick jet. The condition is similar to very high Oh. When We increases to 95, the retraction of the crater base with a concave downward shape can be observed. However, as the retraction of the crater sidewalls is stronger than the retraction of the base, it prevents the further retraction of the crater base and pushes it in the downward direction. This creates favorable conditions for the bubble entrapment process. The sidewalls converge at the symmetry axis above the crater base and a bubble is entrapped at the bottom of the crater. The base of the crater retracts only after the pinch-off of the entrapped bubbles, and it appears as a thin jet above the interface. Compared to We = 95, the movement of the crater base in the downward direction decreases with increases in We to 110. Although the crater sidewalls are able to merge above the crater base, the size of the entrapped bubble decreases. When We increases further to 120, the retraction rate of the crater base becomes stronger than that of the crater sidewalls. Consequently, the sidewalls converge at the base of the retracting crater, and the bubble cannot be entrapped.

IV. CONCLUSIONS

In the present study, we have investigated the impact of a liquid drop on a liquid pool at different impact conditions. This thorough examination has led to the identification and characterization of many regimes, subregimes, and accompanying flow structures. The regimes have been characterized

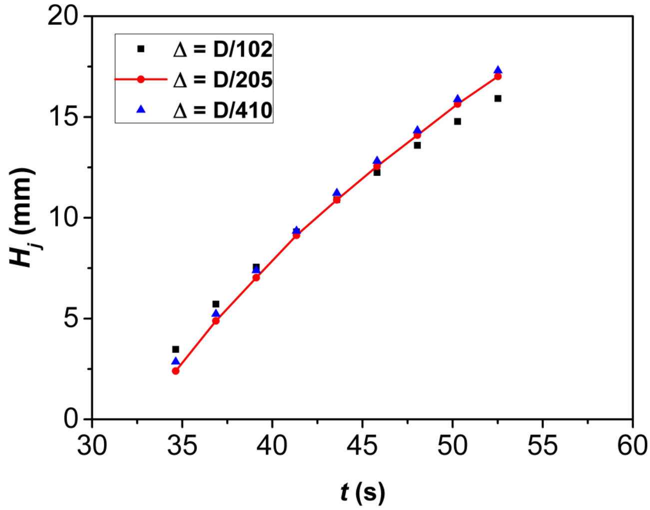

FIG. 22. Variation jet height with time for different grid refinement levels. A 3 mm water drop impacts on a liquid pool from an impingement height of 500 mm (Fr = 333.31, We = 406.12).

by We and Oh based on the interplay of inertia, surface tension, and viscous force. An increase in We and Oh favors (hinders) the complete (partial) coalescence of the drop as they increase the vertical collapse rate compared to the horizontal collapse rate of the drop. As the vortex ring has been observed in both the splashing and coalescence regimes, the boundary between the splashing and coalescence regimes has been defined based on the formation of the jet. The boundary has been determined quantitatively as $\mathrm{We}_{\mathrm{Cco}} = 363.5\mathrm{Oh}^{0.321}$ for $0.002 \leqslant \mathrm{Oh} \leqslant 0.020$. By examining the temporal evolution of the crater, we have ascertained that the competition between the horizontal and vertical collapse rates of the crater determines the occurrence of the regular bubble entrapment. As the momentum of the capillary waves controls both collapse rates, the regular bubble entrapment region has been observed at specific conditions of We and Oh. Accordingly, its lower and upper limits have been determined as $\mathrm{We}_l = 516.6\mathrm{Oh}^{0.273}$ and $\mathrm{We}_u = 694.1\mathrm{Oh}^{0.391}$, respectively, for $0.002 \leqslant \mathrm{Oh} \leqslant 0.020$.

Four new flow structures, namely (i) blob; (ii) blob and secondary ring; (iii) primary ring, secondary ring, and jet; and (iv) primary ring and jet have been brought out along with four previously reported flow behaviors in these regimes. We have found that the generation process of the secondary ring in the coalescence and splashing regimes is different. In the coalescence regime, its origin depends on the dynamics of the cylindrical column that penetrates the pool through the vertex of the crater, whereas in the splashing regime, it depends on the dynamics of the retracting crater. We have also observed that the dynamics of the retracting crater play a significant role in the formation of the jet and inhibition of the primary ring. As the genesis of the flow structures relies on the delicate interplay of inertia, surface tension, and viscous forces, their thresholds have been quantified in terms of We and Oh. Subsequently, a comprehensive classification of them as a function of these controlling dimensionless numbers has been presented as a phase diagram in the novel We-Oh parameter space. This study is expected to help identify the precise impact conditions within which each phenomenon occurs, allowing it to be avoided or permitted depending on the application.

APPENDIX A: GRID INDEPENDENCE STUDY

To study the grid independence study of the simulation, the temporal evolution of jet height H_j for different cell sizes ($\Delta = D/102$–$D/410$) has been compared, as shown in Fig. 22. From the

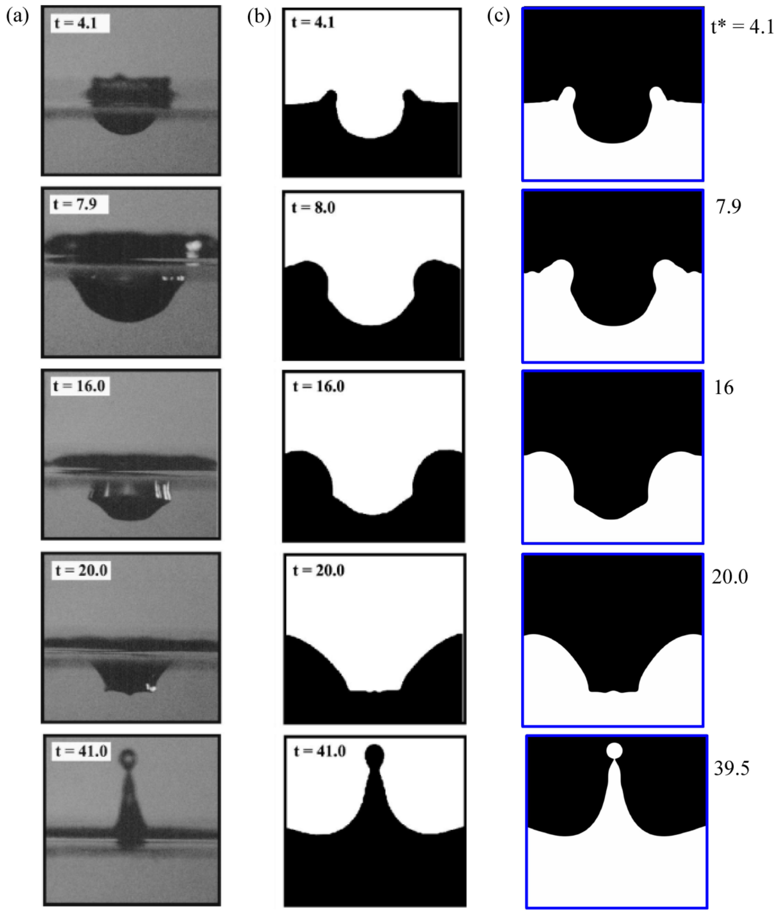

FIG. 23. Qualitative validation of our numerical results (c) with the experimental results (a) and numerical simulations (b), both from Morton *et al.* [34]. A 2.9 mm water drop impinges on a liquid pool from a height of 170 mm (Fr = 85, We = 96).

figure, it can be stated that the temporal evolution of the jet for different cell sizes is similar. Thus, the cell size $\Delta = D/205$ has been used in the present numerical study to reduce computational time.

APPENDIX B: VALIDATION OF THE NUMERICAL RESULT

To validate the present numerical simulation, we compare our numerical results with the corresponding experimental results of Morton *et al.* [34] (as shown in Fig. 23), who have studied the dynamics of a jet during the impingement of a liquid drop on a pool. Figures 23(a) and 23(b) represent, respectively, the experimental and numerical results of Morton *et al.* [34], whereas Fig. 23(c) shows the present numerical results. It can be seen from the figure that our simulation has captured well the crater dynamics to jet formation observed in their experiment for the same impact conditions. The present numerical simulation has also been validated with the experimental and numerical results of Thoraval *et al.* [49] in Fig. 24. The simulation parameters are obtained from their experimental conditions. The graph demonstrates that the bubble entrapment process was captured well using the specified refining levels.

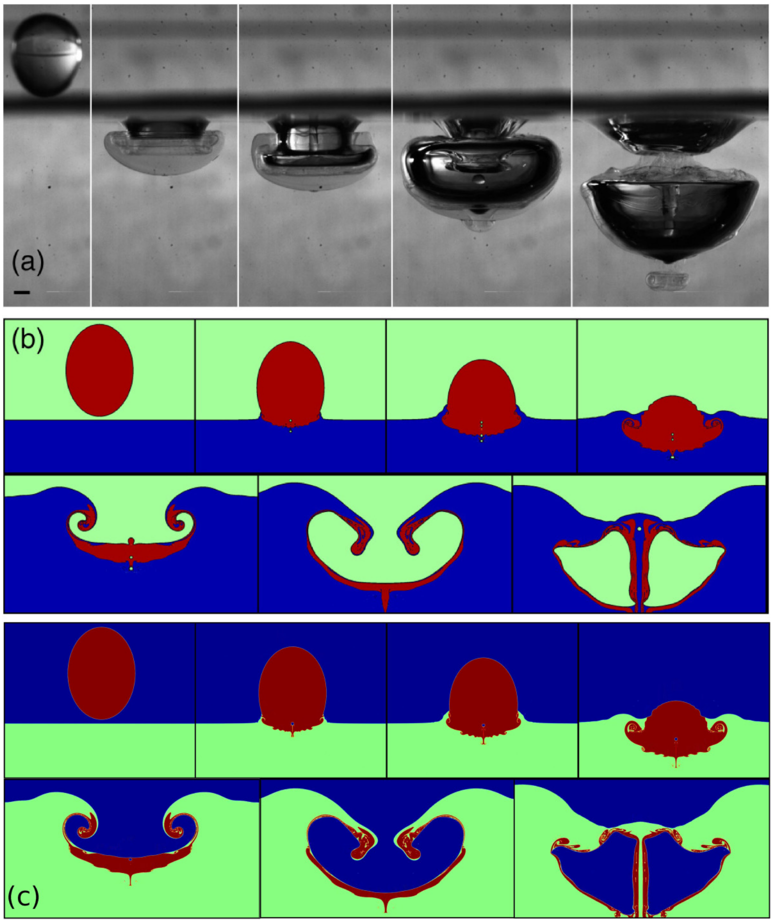

FIG. 24. Qualitative comparison of the present numerical results (c) with the experimental results (a) and numerical simulations (b) of Thoraval *et al.* [49] for a prolate drop, $D = 5\,\mathrm{mm}$, $U = 1.30\,\mathrm{m/s}$.

For quantitative validation purposes, we compare our numerical results with the experimental results of Oğuz and Prosperetti [43], as shown in Fig. 18. Our data points are within their proposed limits.

[1] A. Prosperetti, L. A. Crum, and H. C. Pumphrey, The underwater noise of rain, J. Geophys. Res. **94**, 3255 (1989).

[2] R. Guigon, J.-J. Chaillout, T. Jager, and G. Despesse, Harvesting raindrop energy: Experimental study, Smart Mater. Struct. **17**, 015039 (2008).

[3] G. L. Sainsbury and I. C. Cheeseman, Effect of rain in calming the sea, Nature (London) **166**, 79 (1950).

[4] M. Tsimplis, Effect of rain in calming the sea, J. Phys. Oceanogr. **22**, 404 (1991).

[5] A. V. Anilkumar, C. P. Lee, and T. G. Wang, Surface-tension-induced mixing following coalescence of initially stationary drops, Phys. Fluids A **3**, 2587 (1991).

[6] H. N. Oğuz and A. Prosperetti, Numerical calculation of the underwater noise of rain, J. Fluid Mech. **228**, 417 (1991).

[7] M. R. Behera, S. R. Varade, P. Ghosh, P. Paul, and A. S. Negi, Foaming in micellar solutions: Effects of surfactant, salt, and oil concentrations, Ind. Eng. Chem. Res. **53**, 18497 (2014).
[8] G. E. Charles and S. G. Mason, The mechanism of partial coalescence of liquid drops at liquid/liquid interfaces, J. Colloid Sci. **15**, 105 (1960).
[9] G. E. Charles and S. G. Mason, The coalescence of liquid drops with flat liquid/liquid interfaces, J. Colloid Sci. **15**, 236 (1960).
[10] Z. Mohamed-Kassim and E. K. Longmire, Drop impact on a liquid-liquid interface, Phys. Fluids **15**, 3263 (2003).
[11] Z. Mohamed-Kassim and E. K. Longmire, Drop coalescence through a liquid/liquid interface, Phys. Fluids **16**, 2170 (2004).
[12] H. Aryafar and H. P. Kavehpour, Drop coalescence through planar surfaces, Phys. Fluids **18**, 072105 (2006).
[13] F. Blanchette and T. P. Bigioni, Partial coalescence of drops at liquid interfaces, Nat. Phys. **2**, 254 (2006).
[14] F. Blanchette and T. P. Bigioni, Dynamics of drop coalescence at fluid interfaces, J. Fluid Mech. **620**, 333 (2009).
[15] E. M. Honey and H. P. Kavehpour, Astonishing life of a coalescing drop on a free surface, Phys. Rev. E **73**, 027301 (2006).
[16] S. T. Thoroddsen and K. Takehara, The coalescence cascade of a drop, Phys. Fluids **12**, 1265 (2000).
[17] K. Sun, P. Zhang, Z. Che, and T. Wang, Marangoni-flow-induced partial coalescence of a droplet on a liquid/air interface, Phys. Rev. Fluids **3**, 023602 (2018).
[18] J. J. Thomson and H. F. Newall, On the formation of vortex rings by drops falling into liquids, and some allied phenomena, Proc. R. Soc. London **39**, 417 (1885).
[19] D. S. Chapman and P. R. Critchlow, Formation of vortex rings from falling drops, J. Fluid Mech. **29**, 177 (1967).
[20] F. Rodriguez and R. Mesler, The penetration of drop-formed vortex rings into pools of liquid, J. Colloid Interface Sci. **121**, 121 (1988).
[21] J. S. Lee, S. J. Park, J. H. Lee, B. M. Weon, K. Fezzaa, and J. H. Je, Origin and dynamics of vortex rings in drop splashing, Nat. Commun. **6**, 8187 (2015).
[22] M. R. Behera, A. Dasgupta, and S. Chakraborty, On the generation of vorticity and hydrodynamics of vortex ring during liquid drop impingement, Phys. Fluids **31**, 082108 (2019).
[23] M. R. Behera, A. Dasgupta, and S. Chakraborty, Viscous diffusion induced evolution of a vortex ring, Phys. Fluids **33**, 032116 (2021).
[24] F. Durst, Penetration length and diameter development of vortex rings generated by impacting water drops, Exp. Fluids **21**, 110 (1996).
[25] F. Rodriguez and R. Mesler, Some drops don't splash, J. Colloid Interface Sci. **106**, 347 (1985).
[26] B. Peck and L. Sigurdson, The vortex ring velocity resulting from an impacting water drop, Exp. Fluids **18**, 351 (1995).
[27] P. N. Shankar and M. Kumar, Vortex rings generated by drops just coalescing with a pool, Phys. Fluids **7**, 737 (1995).
[28] J. R. Saylor and N. K. Grizzard, The effect of surfactant monolayers on vortex rings formed from an impacting water drop, Phys. Fluids **15**, 2852 (2003).
[29] A. M. Worthington, On the forms assumed by drops of liquids falling vertically on a horizontal plate, Proc. R. Soc. London **25**, 261 (1877).
[30] A. M. Worthington, *A Study of Splashes* (Longmans Green and Company, New York, 1908).
[31] A. M. Worthington, *The Splash of a Drop* (Society for Promoting Christian Knowledge, London, 1895).
[32] A. M. Worthington, On impact with a liquid surface, Proc. R. Soc. London **34**, 217 (1883).
[33] M. Rein, The transitional regime between coalescing and splashing drops, J. Fluid Mech. **306**, 145 (1996).
[34] D. Morton, M. Rudman, and L. Jong-Leng, An investigation of the flow regimes resulting from splashing drops, Phys. Fluids **12**, 747 (2000).
[35] L. J. Leng, Splash formation by spherical drops, J. Fluid Mech. **427**, 73 (2001).
[36] B. Ray, G. Biswas, and A. Sharma, Regimes during liquid drop impact on a liquid pool, J. Fluid Mech. **768**, 492 (2015).

[37] E. Castillo-Orozco, A. Davanlou, P. K. Choudhury, and R. Kumar, Droplet impact on deep liquid pools: Rayleigh jet to formation of secondary droplets, Phys. Rev. E **92**, 053022 (2015).

[38] R. W. Cresswell and B. R. Morton, Drop-formed vortex rings—the generation of vorticity, Phys. Fluids **7**, 1363 (1995).

[39] M. Hsiao, S. Lichter, and L. G. Quintero, The critical weber number for vortex and jet formation for drops impinging on a liquid pool, Phys. Fluids **31**, 3560 (1988).

[40] S. L. Manzello and J. C. Yang, The influence of liquid pool temperature on the critical impact weber number for splashing, Phys. Fluids **15**, 257 (2003).

[41] G. J. Michon, C. Josserand, and T. Séon, Jet dynamics post drop impact on a deep pool, Phys. Rev. Fluids **2**, 023601 (2017).

[42] H. C. Pumphrey and P. A. Elmore, The entrainment of bubbles by drop impacts, J. Fluid Mech. **220**, 539 (1990).

[43] H. N. Oğuz and A. Prosperetti, Bubble entrainment by the impact of drops on liquid surfaces, J. Fluid Mech. **219**, 143 (1990).

[44] P. A. Elmore, G. L. Chahine, and H. N. Oguz, Cavity and flow measurements of reproducible bubble entrainment following drop impacts, Exp. Fluids **31**, 664 (2001).

[45] Q. Deng, A. V. Anilkumar, and T. G. Wang, The role of viscosity and surface tension in bubble entrapment during drop impact onto a deep liquid pool, J. Fluid Mech. **578**, 119 (2007).

[46] S. Chen and L. Guo, Viscosity effect on regular bubble entrapment during drop impact into a deep pool, Chem. Eng. Sci. **109**, 1 (2014).

[47] S. Popinet, Gerris: A tree-based adaptive solver for the incompressible euler equations in complex geometries, J. Comput. Phys. **190**, 572 (2003).

[48] S. Popinet, An accurate adaptive solver for surface-tension-driven interfacial flows, J. Comput. Phys. **228**, 5838 (2009).

[49] M. J. Thoraval, Y. Li, and S. T. Thoroddsen, Vortex-ring-induced large bubble entrainment during drop impact, Phys. Rev. E **93**, 033128 (2016).

[50] C. Josserand, P. Ray, and S. Zaleski, Droplet impact on a thin liquid film: Anatomy of the splash, J. Fluid Mech. **802**, 775 (2016).

[51] M. R. Behera, A. Dasgupta, and S. Chakraborty, Investigation of regimes during partial/complete coalescence of a liquid drop on a liquid pool, Chem. Eng. Sci. **251**, 117460 (2022).

[52] F. Marcotte, G. J. Michon, T. Séon, and C. Josserand, Ejecta, Corolla, and Splashes from Drop Impacts on Viscous Fluids, Phys. Rev. Lett. **122**, 014501 (2019).

[53] S. Gekle and J. M. Gordillo, Generation and breakup of worthington jets after cavity collapse. Part 1. Jet formation, J. Fluid Mech. **663**, 293 (2010).

[54] See Supplemental Material at http://link.aps.org/supplemental/10.1103/PhysRevFluids.8.014002 for the flow structures observed in the partial coalescence regimes.